Earth, Planets and Space

EXPRESS LETTER

Open Access

Source fault model of the 2018 M_w 5.6 northern Osaka earthquake, Japan, inferred from the aftershock sequence

Aitaro Kato* and Taku Ueda

Abstract

We reconstructed the spatiotemporal evolution of seismicity associated with the 2018 M_w 5.6 northern Osaka earthquake, Japan, to discuss the source fault model of the mainshock rupture, the possible link between this rupture and known active faults, and subsequent crustal deformation. We first relocated the hypocenters listed in the earthquake catalog determined by the Japan Meteorological Agency using a double-difference relocation algorithm. We then searched for the earthquake waveforms that closely resembled those of the relocated hypocenters by applying a matched filtering technique to the continuous waveform data. The relocated hypocenters revealed two distinct planar alignments with different fault geometries. A combination of the relocated hypocenters and focal mechanisms suggests that the mainshock rupture initiated on a NNW–SSE-striking thrust fault, dipping ~45° to the east, with the rupture propagating to an adjacent sub-vertical ENE–WSW-striking strike-slip fault ~0.3 s after the initial mainshock rupture, resulting in the simultaneous propagation of dynamic rupture along the two faults. The strike-slip fault is oblique to the strike of the Arima-Takatsuki Fault, indicating that blind strike-slip faulting occurred. While the east-dipping thrust fault is located deeper than the modeled extent of the Uemachi Fault, a simple extrapolation of the near-surface geometry of the Uemachi fault partially overlaps the mainshock rupture area. Although it is unclear as to whether a blind thrust fault or a deep portion of the Uemachi Fault ruptured during this mainshock–aftershock sequence, a mainshock rupture would have transferred a static stress change of > 0.1 MPa to a portion of the east-dipping thrust fault system. Intensive aftershocks have persisted along the northern and southern edges of the source area, including moderate-magnitude events, whereas the seismicity in the central part of the source area has shown a rapid decay over time. Delayed triggered aftershocks were clearly identified along the northern extension of the rupture area. Because the background seismicity is predominant in this northern area, we interpret that aseismic deformation, such as cataclastic flow lubricated by crustal fluids, triggered this off-fault seismicity.

Keywords: 2018 northern Osaka earthquake, Foreshock, Aftershock, Source fault model, Relocation, Matched filter technique, Background seismicity, Stress transfer

Introduction

The 2018 M_w 5.6 northern Osaka earthquake (M_j (Japan Meteorological Agency (JMA) magnitude) 6.1) is a shallow crustal earthquake that occurred at ~12 km depth along the northeastern edge of the Osaka Plain, Japan, at 0758 JST (JST = UTC + 9 h) on 18 June 2018. Several towns in Osaka Prefecture experienced strong shaking (JMA seismic intensity of 6-lower) due to the mainshock rupture that resulted in serious structural damage and four fatalities. The compressional (P-) wave first-motion data suggest mainshock rupture along a thrust fault with an approximately N–S strike, whereas the centroid moment tensor solution indicates a large non-double-couple component that is characterized as a combination of thrust and strike-slip motion (Fig. 1).

The focal area is located along the southern edge of the Tamba region (Fig. 1), where intense shallow crustal seismicity (12–13 km depth) has been detected for

*Correspondence: akato@eri.u-tokyo.ac.jp
Earthquake Research Institute, University of Tokyo, 1-1-1 Yayoi, Bunkyo-ku, Tokyo 113-0032, Japan

decades (Iio 1996; Hiramatsu et al. 2000; Omuralieva et al. 2012). This area is located within the Niigata-Kobe Tectonic Zone (Fig. 1), a ~60-km-wide zone of high shear strain rate that extends from Niigata to the Kobe region revealed by the global navigation satellite system (GNSS) Earth Observation Network System (GEONET) (e.g., Nishimura 2017). Small earthquakes have occurred across the entire Tamba region and are not always confined to known faults. The dominant focal mechanisms of this shallow seismicity indicate thrust, strike-slip, and a mixture of these slip regimes, with approximately E–W-oriented P-axes (Iio 1996).

Surface traces of active faults are densely distributed across the Kinki District, including the mainshock source area. The fault traces of major active faults, such as the Arima-Takatsuki (ATF), Ikoma (IKF), and Uemachi (UMF) fault zones, are situated near the source area (Fig. 1) (Sato et al. 2009; Headquarters for Earthquake Research Promotion of MEXT 2018).

The mainshock rupture process of the 2018 northern Osaka earthquake remains poorly understood due to its complex rupture history. Furthermore, there are few constraints on a link between the known surface traces of the major active faults and the source fault at depth, and on crustal deformation after the mainshock. To identify the source fault geometry and understand the subsequent crustal deformation, it is fundamentally important to reveal precise spatial temporal evolution of aftershock

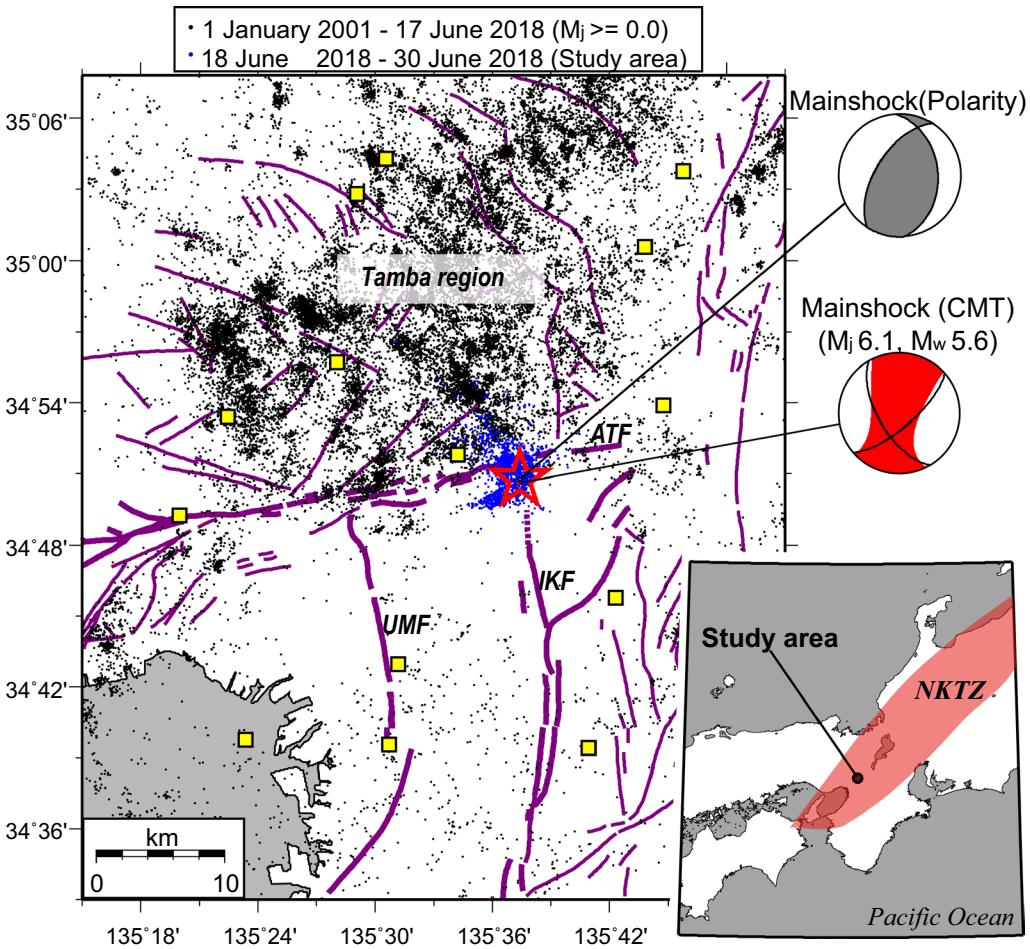

Fig. 1 Tectonic map of the study region and recent seismicity. The red star indicates the mainshock epicenter. The focal mechanism was constrained using the P-wave first-motion data (gray beach ball) and CMT solution (red beach ball) estimated by JMA. The black and blue dots denote the epicenters determined by JMA before (from 1 January 2001 to 17 June 2018) and after (from 18 to 30 June 2018 in the study area) the mainshock rupture, respectively. The yellow squares denote the permanent seismic stations used in the analysis. The Arima-Takatsuki (ATF), Ikoma (IKF), and Uemachi (UMF) fault zones are shown as thick purple lines, and the other major active faults are shown as thin purple lines. The inset shows a regional map of the studied area. NKTZ (red shading) denotes the Niigata–Kobe Tectonic Zone, as identified by the GNSS network (GEONET)

sequence following the 2018 northern Osaka earthquake (e.g., Thurber et al. 2006; Kato et al. 2013a, 2016a).

Here, we relocate the earthquakes associated with the mainshock rupture applying a double-difference relocation algorithm (e.g., Waldhauser and Ellsworth 2000) to differential travel time data. To expand the earthquake dataset, we then apply a matched filter technique (e.g., Shelly et al. 2007) to the continuous waveform data, using the relocated earthquakes as template events. These results provide an excellent opportunity to explore the mainshock rupture dynamics of the region, including the relationship between active faults and the mainshock, and the delayed triggered seismicity at the northern extension of the source area.

Methods

We relocated earthquakes included in the JMA catalog that occurred between 17 and 30 June 2018, using the waveform data recorded at 14 seismic stations near the mainshock hypocenter (Fig. 1). These 14 seismic stations (a spacing of ~10–20 km) are operated by NIED (National Research Institute for Earth Science and Disaster Resilience), Kyoto University, and JMA. We used the P- and shear (S-) wave arrival time data for the seismic stations that were determined by JMA. Furthermore, we applied an automatic processing (Horiuchi 2015) to the waveform data from the seismic stations that were not analyzed by JMA to obtain additional arrival time data. The earthquakes with a sufficient number of arrival times (i.e., the numbers of P- and S-wave arrivals must both be greater than 6) were then selected for the relocation step. We applied a double-difference relocation algorithm (Waldhauser and Ellsworth 2000; Zhang and Thurber 2003) to differential times constructed by picking (280,472 data) and waveform cross-correlation method (547,290 data with cross-correlation coefficient ≥ 0.85), using station corrections estimated by averaging values of travel time residuals at each station and assuming the one-dimensional velocity structure routinely used in the JMA location procedure. The correlation measurements were conducted for all possible pairs using a 2.4-s window (4–12 Hz bandpass-filtered) beginning 1.2 s before the manually picked arrival time. We relocated 2182 earthquakes in the study area via this process (Figs. 1, 2). The weighted rms residual of the cross-correlation data decreased from 55 to 2 ms, and that of the picked data reduced from 91 to 35 ms after relocation. The relative location errors (2σ) in the horizontal and vertical directions are estimated to be 0.24 km and 0.7 km, respectively, based on jackknife test that randomly removes arrival time data of four stations among all the stations (200 trials).

To investigate the spatiotemporal evolution of the local seismicity more precisely, we applied the matched filter technique (Kato et al. 2013b) to the continuous waveform data recorded between 17 and 30 June 2018, using the 2182 relocated earthquakes as template events. The continuous and template waveforms from 14 seismic stations were first preprocessed using a 4–12 Hz bandpass filter and downsampling from 100 to 50 Hz. We then extracted a 5.0 s window starting 2.0 s before the synthetic P-wave on the vertical-component and 2.0 s before the synthetic S-wave on the two horizontal components. The synthetic arrival times were calculated using the JMA one-dimensional velocity structure.

The threshold for event detection was set at 9.5 times the median absolute deviation of the average correlation coefficient calculated over the day of interest. This threshold was chosen based on a visual inspection of the detected events. We assigned the location of the detected event to that of the template event and computed the magnitude of the detected event based on the median value of the maximum amplitude ratios at each channel between the template and detected events. Finally, we obtained 11,114 earthquakes via this matched filter technique, which is more than four times the number of events in the JMA catalog during the same period (2628 events), thereby yielding a significant improvement in the completeness of magnitude (down to -0.1).

Previous studies have indicated that temporal changes in the background rate of seismicity often exhibit a good correlation with transient aseismic processes, such as slow slip and fluid intrusion (e.g., Hainzl and Ogata 2005; Kato et al. 2016b; Reverso et al. 2016). To extract transient aseismic process after the mainshock rupture, we computed the temporal change in the background seismicity rate by applying the stochastic declustering method based on the space–time ETAS (epidemic-type aftershock sequence) model (Zhuang et al. 2002, 2004) to the newly constructed earthquake catalog by the matched filter technique ($M \geq 1.0$). After fitting the entire time series of the seismicity rate via the space–time ETAS model (parameter values: $A = 9.41 \times 10^{-1}$ events, $c = 4.12 \times 10^{-3}$ days, $\alpha = 1.17$ M^{-1}, $p = 1.04$, $D = 6.06 \times 10^{-4}$, $q = 1.98$, and $\gamma = 1.07 \times 10^{-1}$ M^{-1}), we calculated the probability of each earthquake being either a background event or an offspring (cluster) event that was triggered by other events. We then conducted a stochastic classification of the earthquakes by comparing the probability of each earthquake being background with a random number (from 0 to 1). After averaging the number of background events for the 1000 stochastically classified time series, we estimated the temporal change of the background rate.

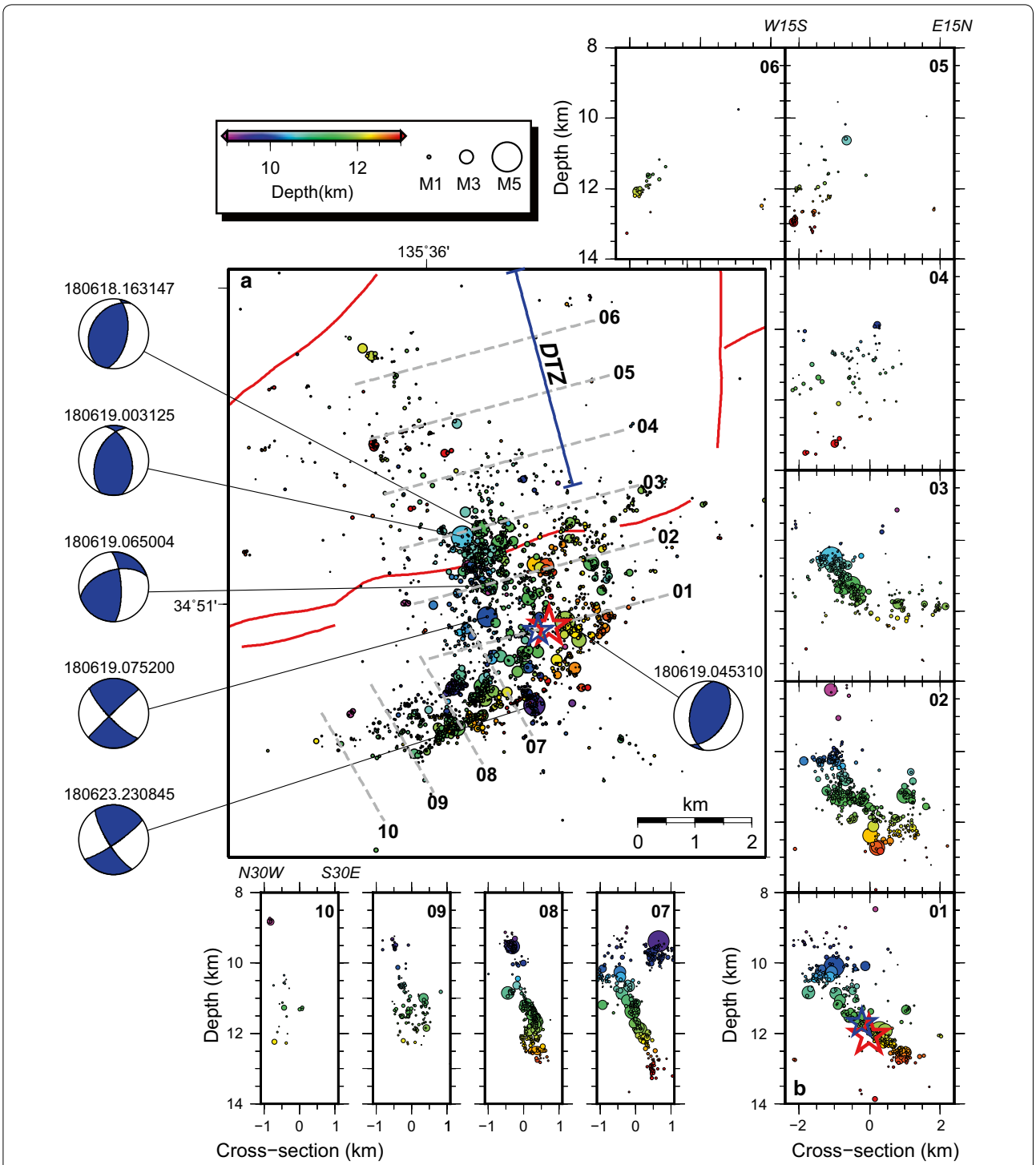

Fig. 2 Relocated earthquakes associated with the 2018 M_w 5.6 northern Osaka earthquake. **a** Map view of the relocated epicenters, which are shown as circles that are scaled to earthquake magnitude and colored to hypocentral depth. The blue beach balls denote the aftershock focal mechanisms estimated by NIED (origin time is above each beach ball, in YYMMDD.HHMMSS format). The blue and red stars are the epicenters of the foreshock and mainshock event, respectively. The red lines denote the surface traces of active faults in the area. DTZ indicates the zone with delayed triggered aftershocks (see text). **b** Depth sections of the relocated hypocenters along the profiles shown in Fig. 2a

Results

The relocated epicenters are distributed along two distinct linear orientations that extend from the mainshock epicenter (Fig. 2a). The epicenters to the north of the mainshock epicenter are broadly distributed along a N15W–S15E orientation, with the depth sections indicating a plane dipping ~45° to the east (sections 01–03 in Fig. 2b). The width of the aftershock distribution narrows near the hypocenter of the mainshock rupture (section 01 in Fig. 2b). However, the northern extension of the aftershock distribution is sporadic and aligns along a conjugate west-dipping fault plane (sections 05 and 06 in Fig. 2b). Conversely, the epicenters to the south of the mainshock hypocenter are tightly aligned along an ENE–WSW-striking plane. The depth sections indicate a fault plane dipping steeply (70°–80°) to the southeast (sections 07–10 in Fig. 2b). This fault plane is adjacent to a fault plane near the mainshock hypocenter that dips at ~45° toward the east, but the two fault planes do not appear to intersect.

The spatiotemporal evolution of the seismicity detected by the matched filter technique reveals that intensive aftershocks persisted along the northern and southern edges of the source area, including moderate-magnitude events, whereas the seismicity in the central part of the source area rapidly decayed over time (Fig. 3a). The JMA catalog shows a similar pattern, but the contrast is less conspicuous because of the sparser data coverage.

Furthermore, we observe a delayed increase in seismicity to the north of the source area, which we term the delayed triggered zone (DTZ), with seismicity slowly propagating to the north within a day of the mainshock rupture (Fig. 3a). The earliest event within the DTZ occurred ~2.5 h after the mainshock rupture. The ratio of cumulative background events to a total number of the DTZ gradually increased over time, reaching a maximum value of ~60% at the end of the study period, with a slight acceleration at ~1 week after the mainshock rupture (blue curve in Fig. 3b). Conversely, the contribution of the background seismicity to the total seismicity in the mainshock rupture area was quite small and relatively constant over time (black curve in Fig. 3b).

There was minimal foreshock activity during the 2 days prior to the mainshock rupture (Fig. 3a). One M_j 0.9 foreshock occurred to the west and updip of the mainshock hypocenter, preceding the mainshock rupture by ~7 h (blue star in Figs. 2, 3). The relative distance between these two events is ~400 m. However, no further significant seismic activity was detected between the foreshock and mainshock ruptures, even after applying the matched filter technique.

Discussion

The relocated aftershocks reveal lateral variations between the two adjacent fault planes, which are a NNW–SSE-striking thrust fault (F1) that dips ~45° to the east and a sub-vertical ENE–WSW-striking strike-slip fault (F2), in the vicinity of the mainshock hypocenter (Figs. 2, 4). The mainshock rupture initiated along the F1 fault and near the F2 fault. Furthermore, the focal mechanism derived from the P-wave first-motion data suggests thrust faulting, whereas the centroid moment tensor of the mainshock indicates a large non-double-couple component (Fig. 1). The focal mechanisms of the major aftershocks indicate a mixture of thrust and strike-slip faulting, within a stress field dominated by E–W compression (Fig. 2). We therefore interpret that the mainshock rupture initiated along the F1 fault and transitioned to the adjacent F2 fault, resulting in the simultaneous propagation of dynamic rupture along the two different fault geometries (Fig. 4). Since the distance between the mainshock hypocenter and the eastern edge of the F2 fault is less than 1 km, the rupture along the F2 fault may have been delayed by ~0.3 s, assuming a mainshock rupture velocity of 3 km s^{-1}. This source fault structure is basically consistent with a kinematic slip model that was derived from strong ground motion data (Asano 2018).

We then attempt to model the mainshock CMT solution as a combination of the two double-couple moment tensors found for the F1 and F2 faults. We searched the best combination of the two moment tensors, varying the dip- and rake-angles and the moment ratio, keeping the strike of the F1 and F2 fault to be 345° and 60°, respectively. That's because the fault-strike is the best constrained parameter. A combination of two moment tensors (F1: strike = 345°, dip = 50°, rake = 85°, M_w 5.3; F2: strike = 60°, dip = 80°, rake = 160°, M_w 5.5) closely resembles the mainshock CMT solution (Fig. 4b).

The simultaneous rupture of the thrust and strike-slip faults is a physically plausible in some cases, given the approximately E–W horizontal orientation of the maximum principal stress axis and the comparable absolute amplitudes of the intermediate and minimum principal stresses in the Kinki District (Iio 1996). This is in agreement with previous studies that have inferred simultaneous rupture along two conjugate fault planes in deformed intraplate regions (e.g., Aochi and Kato 2010; Aoi et al. 2010). Note that the present study clarifies the mainshock rupture history of the 2018 M_w 5.6 northern Osaka earthquake, with rupture initiating on the thrust fault and then propagating along both the thrust and strike-slip faults. Recent high-resolution observations of the 2016 M_w 7.8 Kaikōura earthquake, New Zealand, have highlighted the complex multi-fault rupture of at least 12 major

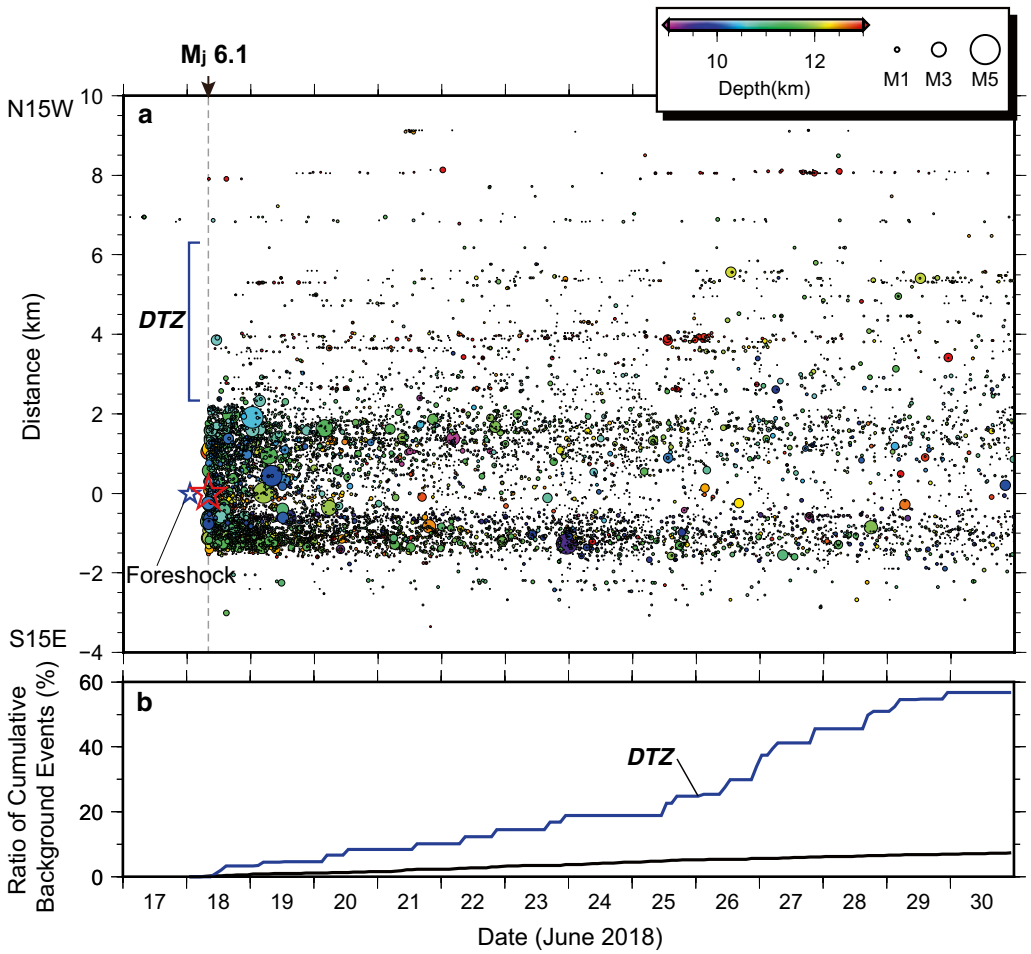

Fig. 3 Spatiotemporal evolution of seismicity revealed via the matched filter technique. **a** Space–time diagram of the detected events, which are shown as circles that are scaled to earthquake magnitude and colored to hypocentral depth. The blue and red stars denote the foreshock and mainshock events, respectively. DTZ indicates the zone with delayed triggered aftershocks. **b** Time series of the ratio of the cumulative number of background events to the total events in the two following areas. Blue curve: 2.3 km < *Y* < 6.3 km (DTZ). Black curve: −4 km < *Y* < 2.3 km. Note that the mainshock event is located at *Y* = 0 km. Background events are earthquakes that were not triggered by other earthquakes. See the "Methods" section for further details

fault planes, with a mixture of thrust and strike-slip fault movements (e.g., Hamling et al. 2017). Therefore, the simultaneous rupture of two different faulting styles during the Osaka earthquake is not unrealistic.

These recent observations indicate the potential for rupture propagation across different faulting styles, which is particularly important in terms of seismic hazard analysis. The long-term probability of earthquake generation for each major thrust and strike-slip fault in the Kinki District has been evaluated by the Headquarters for Earthquake Research Promotion of MEXT, but the possibility of rupture propagation across adjacent thrust and strike-slip faults has not been incorporated into the evaluation. Since the stress field in the Kinki District can promote both thrust and strike-slip faulting, as mentioned above, it is important to consider the possibility of simultaneous dynamic rupture along adjacent fault planes in future seismic hazard analyses.

The surface fault traces of several major active faults are observed near the source area (Fig. 1). The horizontal distance between the source area and ATF/IKF is quite short. However, the F2 fault is oblique to the ATF (Fig. 2), and the south-dipping F2 fault does not align with the north-dipping ATF. Seismic reflection profiling along a 135-km line from Osaka to the Ise Basin suggests that near the surface, the IKF dips ~30° to the east (Sato et al. 2009). If we simply extend this east-dipping fault to depth, the inferred downdip section of the IKF is located far from the source area of the Osaka earthquake (Fig. 5a). The above information therefore suggests that

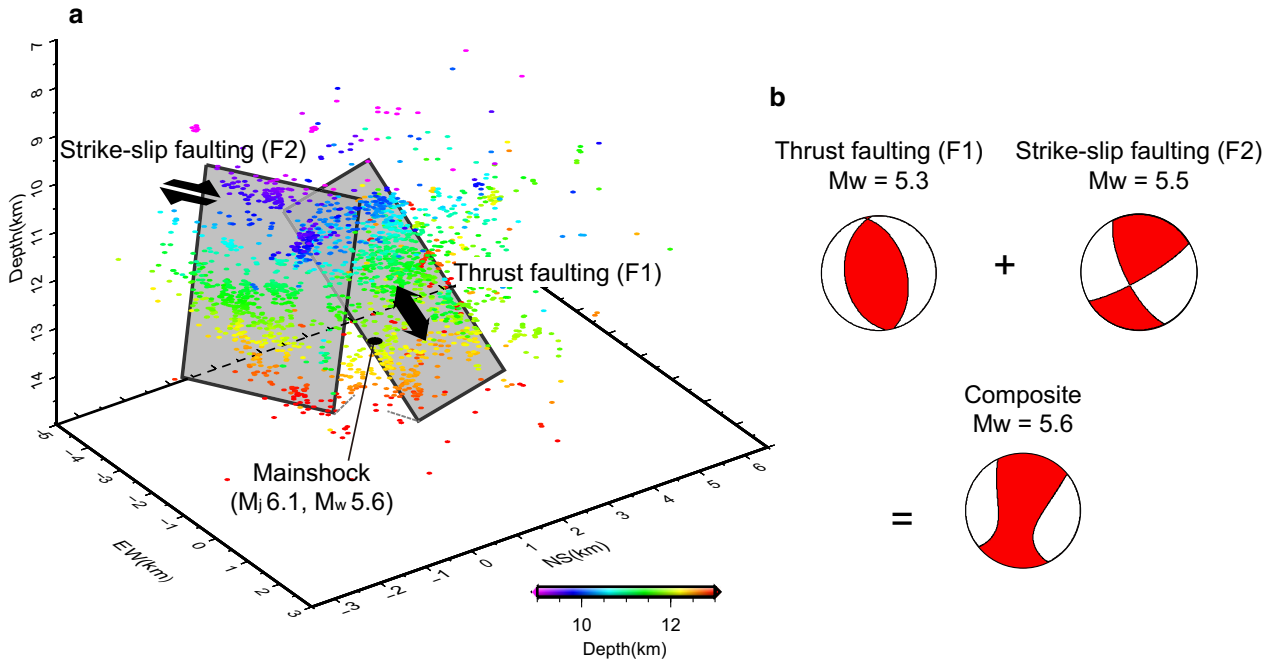

Fig. 4 Source fault model of the mainshock rupture. **a** Perspective view of the relocated aftershocks (colored to depth) and the inferred fault orientations. The two gray rectangles represent the NNW–SSE-striking thrust dipping to the east (F1) and the sub-vertical, ENE–WSW-striking strike-slip fault (F2). **b** The best combination of two double-couple moment tensors found for the F1 and F2 faults to explain the observed mainshock CMT solution (F1: strike = 345°, dip = 50°, rake = 85°, F2: strike = 60°, dip = 80°, rake = 160°)

the mainshock rupture did not occur along the ATF or IKF.

Near the surface, the UMF dips ~40° to the east (Sato et al. 2009). Sato et al. (2009) proposed that the UMF merges with a possible mid-crustal horizontal detachment below Minakuchi Hills at deep depths (eastward extension of the black dashed lines in Fig. 5a), thereby explaining the gentle eastward tilting of the basement beneath the Osaka Plain. This interpretation means that the mainshock area may be deeper than the horizontal detachment by several kilometers, indicating in turn the reactivation of a different fault system during the mainshock rupture. Alternatively, a simple extension of the near-surface trend of the UMF appears to intersect the F1 fault to the north of the mainshock hypocenter (blue dashed line in Fig. 5a). The F1 fault may therefore be a downdip extension of the UMF. In either interpretation, the less-constrained trajectory of the UMF at depth obscures the relationship between the mainshock rupture area and the deep geometry of the UMF.

To assess the possibility of a triggered earthquake on nearby faults, we calculated Coulomb stress change resolved on east-dipping thrust fault (strike = 345°, dip = 30°, rake = 90°) by the mainshock rupture, assuming a frictional coefficient of 0.4 and shear modulus of 25 GPa in a uniform elastic half-space with Poisson's ratio of 0.25 (Lin and Stein 2004; Toda et al. 2005). We further assumed a uniform slip of 0.5 m along the two mainshock faults. The mainshock rupture transfers a static stress change greater than 0.1 MPa to parts of the east-dipping thrust system, including the UMF (Fig. 5a). This stress perturbation may boost the earthquake hazard beneath Osaka Plain. It is therefore important to continuously monitor seismicity and geodetic signal in this region using a dense seismic and geodetic network to detect the spatiotemporal evolution of local crustal deformation.

The delayed triggering of aftershocks is clearly identified along the northern extension of the mainshock rupture area (DTZ in Figs. 2, 3). We infer that external forcing, such as fluid migration or aseismic transient deformation, induced this off-fault seismicity, as the ratio of the cumulative background events to a total number of earthquakes in the DTZ gradually increased over time, reaching a maximum value of ~60% at the end of the study period. Hiramatsu et al. (2000) demonstrated that the coda-Q^{-1} values in the Tamba District increased after the 1995 M_w 6.9 Hyogo-ken Nanbu earthquake, accompanied by intensive induced seismicity. They attributed this observation to small-scale heterogeneous damage, with a characteristic length of 100 m, in the crust that was activated by the ~0.02 MPa stress change induced by the Hyogo-ken Nanbu earthquake.

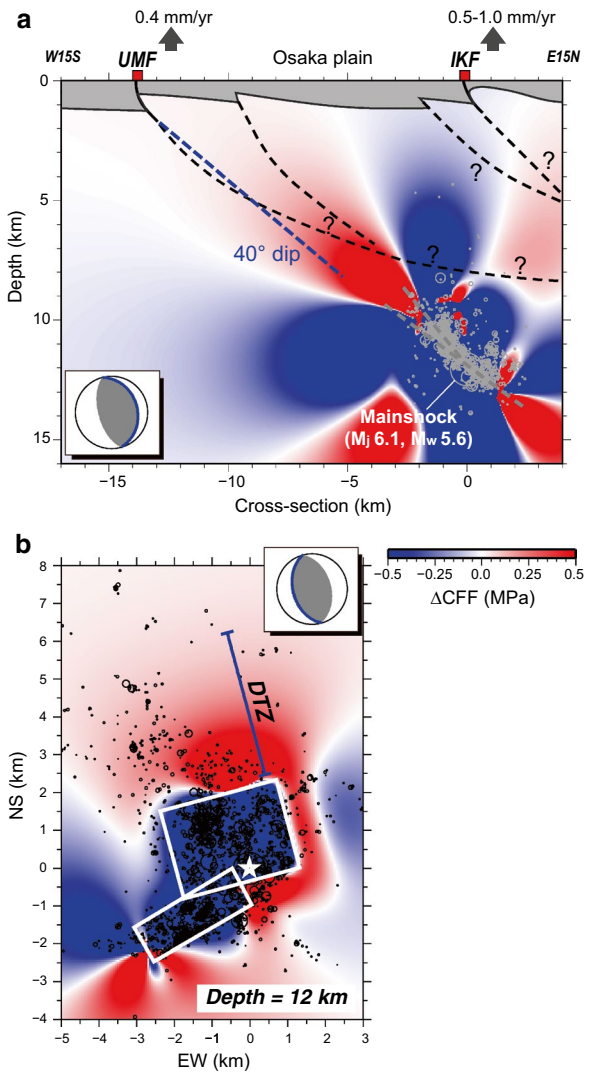

Fig. 5 **a** Seismic diagram showing the fault systems beneath the Osaka Plain along an ENE–WSW profile, superimposed on the Coulomb stress changes resolved on east-dipping thrust fault (strike = 345°, dip = 30°, rake = 90°) induced by the mainshock rupture. The receiver fault is shown as a blue curve in the inset. The black dashed curves denote the deep fault geometries interpreted by Sato et al. (2009). The blue dashed line shows a simple 40°-dipping extension of the UMF near-surface geometry. The gray circles are the relocated hypocenters along cross sections 01–03 in Fig. 2b. The solid arrows denote the reported vertical slip rates of the active faults in mm/year. **b** Calculated Coulomb stress changes at 12 km depth resolved on west-dipping thrust fault (strike = 165°, dip = 45°, rake = 90°) induced by the mainshock rupture. The receiver fault is shown as a blue curve in the inset. DTZ indicates the zone with delayed triggered aftershocks. The white star denotes the mainshock epicenter, and the white rectangles are the two source fault models inferred from the present study

We calculated the Coulomb stress change resolved on a thrust fault (strike = 165°, dip = 45°, rake = 90°) by the 2018 Osaka earthquake (Fig. 5b) (Lin and Stein 2004; Toda et al. 2005). The Osaka mainshock transferred > ~ 0.1 MPa of stress to the northern off-fault area including DTZ, which is much larger than the stress transfer of the Hyogo-ken Nanbu earthquake. Therefore, the stress change could have caused deeper crustal damage, resulting in local weakening of the crust. The local crust may have accommodated some of the accumulated elastic energy thorough aseismic deformation, such as cataclastic flow lubricated by crustal fluids.

Conclusions

We relocated the earthquakes associated with the 2018 northern Osaka mainshock rupture and then applied a matched filter technique to the continuous waveform data, using the relocated earthquakes as template events. The combination of the relocated hypocenters and focal mechanisms suggests that the mainshock rupture initiated on a NNW–SSE-striking thrust fault, dipping ~ 45° to the east, with the rupture propagating to an adjacent sub-vertical ENE–WSW-striking strike-slip fault ~ 0.3 s after the initial mainshock rupture, resulting in the simultaneous propagation of dynamic rupture along the two faults. The two fault planes do not appear to intersect. We then discussed a potential link between the known surface traces of the major active faults and the source fault. Furthermore, delayed triggered aftershocks were clearly identified along the northern extension of the rupture area.

Abbreviations

JMA: Japan Meteorological Agency; GNSS: global navigation satellite system; GEONET: GNSS Earth Observation Network System; ATF: Arima-Takatsuki Fault; IKF: Ikoma Fault; UMF: Uemachi Fault; NIED: National Research Institute for Earth Science and Disaster Resilience; DTZ: delayed triggered zone.

Authors' contributions

AK carried out the data processing, relocation, and matched filter analysis and drafted the manuscript. TU analyzed the seismicity in the present study using a statistical model and helped draft the manuscript. All authors read and approved the final manuscript.

Acknowledgements

We thank NIED, JMA, and Kyoto University for allowing us to use the waveform data collected from their permanent seismic stations. JMA provided the earthquake catalog and direct-wave (P- and S-wave) arrival times. We are grateful to J. Zhuang for providing the space–time ETAS model used in this study.

Competing interests

The authors declare that they have no competing interests.

Availability of data and materials

The data that support the findings of this study are available at the Earthquake Research Institute, University of Tokyo, and the NIED Data Management Center (https://hinetwww11.bosai.go.jp/auth/?LANG=en).

Consent for publication

Not applicable.

Funding
This study was supported by the Ministry of Education, Culture, Sports, Science and Technology of Japan, under its Earthquake and Volcano Hazards Observation and Research Program. This study was also partially supported by JST CREST Grant Number JPMJCR1763 and JSPS KAKENHI Grant Number JP16H06473.

Publisher's Note

Received: 26 October 2018 Accepted: 25 January 2019
Published online: 30 January 2019

References

Aochi H, Kato A (2010) Dynamic rupture of crosscutting faults: a possible rupture process for the 2007 Mw6.6 Niigata-ken Chuetsu-Oki earthquake. J Geophys Res Solid Earth 115:1–10. https://doi.org/10.1029/2009JB006556

Aoi S, Enescu B, Suzuki W et al (2010) Stress transfer in the Tokai subduction zone from the 2009 Suruga Bay earthquake in Japan. Nat Geosci 3:496–500. https://doi.org/10.1038/ngeo885

Asano K (2018) Source process and strong motion of the 2018 northern Osaka earthquake, Japan. http://committees.jsce.or.jp/eec2/system/files/20180723osaka_%E4%BA%AC%E5%A4%A7%E6%B5%85%E9%87%8E.pdf. Accessed 20 Oct 2018

Hainzl S, Ogata Y (2005) Detecting fluid signals in seismicity data through statistical earthquake modeling. J Geophys Res Solid Earth 110:1–10. https://doi.org/10.1029/2004JB003247

Hamling IJ, Hreinsdóttir S, Clark K et al (2017) Complex multifault rupture during the 2016 Mw 7.8 Kaikōura earthquake, New Zealand. Science. https://doi.org/10.1126/science.aam7194

Headquarters for Earthquake Research Promotion of MEXT (2018) Long-term evaluation; Evaluations of active faults. https://www.jishin.go.jp/evaluation/long_term_evaluation/major_active_fault/. Accessed 20 Oct 2018

Hiramatsu Y, Hayashi N, Furumoto M, Katao H (2000) Temporal changes in coda Q−1 and b value due to the static stress change associated with the 1995 Hyogo-ken Nanbu earthquake. J Geophys Res Solid Earth 105:6141–6151. https://doi.org/10.1029/1999JB900432

Horiuchi S (2015) Development of automatic hypocenter location with accuracy compared to manually picking. Paper presented at the 2015 international workshop on earthquake early warning, China Earthquake Administration, Beijing, 5–7 Nov 2015

Iio Y (1996) Depth-dependent change in the focal mechanism of shallow earthquakes: implications for brittle-plastic transition in a seismogenic region. J Geophys Res 101:11209–11216

Kato A, Igarashi T, Obara K et al (2013a) Imaging the source regions of normal faulting sequences induced by the 2011 M9.0 Tohoku-Oki earthquake. Geophys Res Lett 40:273–278. https://doi.org/10.1002/grl.50104

Kato A, Fukuda J, Obara K (2013b) Response of seismicity to static and dynamic stress changes induced by the 2011 M9.0 Tohoku-Oki earthquake. Geophys Res Lett 40:3572–3578. https://doi.org/10.1002/grl.50699

Kato A, Fukuda J, Nakagawa S, Obara K (2016a) Foreshock migration preceding the 2016 Mw7.0 Kumamoto earthquake, Japan. Geophys Res Lett 43:8945–8953. https://doi.org/10.1002/2016GL070079

Kato A, Fukuda J, Kumazawa T, Nakagawa S (2016b) Accelerated nucleation of the 2014 Iquique, Chile Mw 8.2 Earthquake. Sci Rep 6:1–9. https://doi.org/10.1038/srep24792

Lin J, Stein RS (2004) Stress triggering in thrust and subduction earthquakes and stress interaction between the southern San Andreas and nearby thrust and strike-slip faults. J Geophys Res Solid Earth 109:1–19. https://doi.org/10.1029/2003JB002607

Nishimura T (2017) Stain concentration zones in the Japanese islands clarified from GNSS data and its relation with active faults and inland earthquakes. Active Faults 46:33–39. https://doi.org/10.11462/afr.2017.46_33

Omuralieva AM, Hasegawa A, Matsuzawa T et al (2012) Lateral variation of the cutoff depth of shallow earthquakes beneath the Japan Islands and its implications for seismogenesis. Tectonophysics 518–521:93–105. https://doi.org/10.1016/j.tecto.2011.11.013

Reverso T, Marsan D, Helmstetter A, Enescu B (2016) Background seismicity in Boso Peninsula, Japan: long-term acceleration, and relationship with slow slip events. Geophys Res Lett 43:5671–5679. https://doi.org/10.1002/2016GL068524

Sato H, Ito K, Abe S et al (2009) Deep seismic reflection profiling across active reverse faults in the Kinki Triangle, central Japan. Tectonophysics 472:86–94. https://doi.org/10.1016/j.tecto.2008.06.014

Shelly DR, Beroza GC, Ide S (2007) Non-volcanic tremor and low-frequency earthquake swarms. Nature 446:305–307. https://doi.org/10.1038/nature05666

Thurber C, Zhang H, Waldhauser F et al (2006) Three-dimensional compressional wavespeed model, earthquake relocations, and focal mechanisms for the Parkfield, California, region. Bull Seismol Soc Am 96:38–49. https://doi.org/10.1785/0120050825

Toda S, Stein RS, Richards-Dinger K, Bozkurt SB (2005) Forecasting the evolution of seismicity in southern California: animations built on earthquake stress transfer. J Geophys Res Solid Earth 110:1–17. https://doi.org/10.1029/2004JB003415

Waldhauser F, Ellsworth WL (2000) A double-difference earthquake location algorithm: method and application to the Northern Hayward Fault, California. Bull Seismol Soc Am 90:1353–1368. https://doi.org/10.1785/012000006

Zhang H, Thurber CH (2003) Double-difference tomography: the method and its application to the Hayward Fault, California. Bull Seismol Soc Am 93:1875–1889. https://doi.org/10.1785/0120020190

Zhuang J, Ogata Y, Vere-Jones D (2002) Stochastic declustering of space–time earthquake occurrences. J Am Stat Assoc 97:369–380

Zhuang J, Ogata Y, Vere-Jones D (2004) Analyzing earthquake clustering features by using stochastic reconstruction. J Geophys Res Solid Earth 109:1–17. https://doi.org/10.1029/2003JB002879